Technical Paper

Journal of the Society of Navel Architects of Korea
Vol. 27, No. 3, September 1990
大 韓 造 船 學 會 誌
第27卷 第3號 1990年 9月

Prediction of Hydrodynamic Impact Loads on Three-Dimensional Bodies

by

Armin W. Troesch* and Chang-Gu Kang**

3차원 물체에 작용하는 유체동력학적 충격하중추정

Armin W. Troesch*, 강 창 구**

Abstract

The three dimensional aspects of hydrodynamic impact are discussed. Theoretical and experimental results for a sphere and a cusped body are presented. The cusped body is axisymmetric and resembles the bow profile of a ship with flare. The sphere was subjected to both vertical and oblique impact angles while the cusped body experienced only vertical motion. Three dimensional calculations using normal dipole distributions and an equi-potentioal free surface are compared with experimental results. The theoretical boundary value problem was solved using a known interior flow. This procedure reduced computation times significantly. Comparisons between theory and experiment show that, depending upon the body shape theoretical estimates of the maximum impact force may be larger or smaller than the experimental values. But the theoretical estimate can be used for practical purposes.

요 약

본 논문에서는 이론적인 방법과 실험적인 방법에 의해서 구와 플레어 형상을 갖는 축대칭 물체와 같이 3차원 물체에 대한 충격력을 검토하였다. 플레어 형상을 갖는 축대칭물체는 선수와 유사한 형상을 갖고 있다. 플레어 형상물체는 연직운동에 대한 것만을 검토한 반면 구에 대해서는 연직운동만이 아니라 사각 충격에 대해서도 검토하였다. 다이폴분포와 등포텐시얼 자유표면문제를 푼 계산결과와 실험결과를 비교하였다. 경계치문제는 알려진 내부유동을 사용함으로써 계산시간을 단축하였다. 이론과 실험의 비교로부터 물체형상에 따라 최대 충격력의 이론추정치는 실험치보다 더 크거나 작을 수 있다는 것을 보여 주고 있다. 그러나 이론치가 실용적으로 사용될 수 있음을 보여주고 있다.

1. Introduction

The hydrodynamic loads imposed upon a vessel experiencing large amplitude motions can be severe. Structural damage to the forebodies of ships with large flare angles has occurred in head and bow quartering seas indicating that both vertical and horizontal (and possibly torsional) impact loads are important.

Manuscript received: June 4, 1990, revised manuscript received: August 2, 1990
* The University of Michigan, Dept. of Naval Architecture & Marine Engineering
** Member, Korea Research Institute of Ships and Ocean Engineering

While the impact problem has been investigated in various forms for years, most theories have dealt with two-dimensional, vertical aspects. The classical impact problem was formulated by von Karman[21] and modified to include Wagner[22]. These two papers serve as the initial references for much of the later studies. Some authors, such as Payne[17], suggest that the modifications to von Karman's work were not necessarily improvements. Sarpkaya and Isaacson[18] review the literature of ocean engineering applications for von Karman-type impact solutions. These are important when considering the wave-slam on horizontal or nearly horizontal circular cylinders. More recently, the two-dimensional problem including gravitational effects and the non-linear free surace boundary condition has been solved numerically. Yim[26], Gallagher and McGregor[6], and Greenhow[7], among others, have used various numerical time stepping techniques to get good descriptions of two-dimensional wedge impact including the spray jet.

Relatively few attempts have been made to rigorously solve impact problems dealing with three dimensional bodies. Examples of three dimensional solutions are Shiffman and Spencer[19], Chuang[4], and Miloh[12]. Shiffman and Spencer[19] and Chuang[4] developed general expressions for the pressure distributions and slamming forces on a cone. Using similar assumptions, Miloh[12] analytically derived the added mass coefficients for a double spherical bowl. From these coefficients the impact force on a sphere was calculated assuming that the free surface is represented by an equi-potential or zero gravity surface. Miloh[12] or Greenhow[7] offer good reviews of the relevant literature.

Of practical engineering interest are the impact forces in the bow region of a ship. Due to the complexities associated with three-dimensional boundary value problems, it has been common practice to use simplifying assumptions that reduce the calculations of hydrodynamic forces to a two-dimensional strip theory. Examples of this are given by Ochi and Motter[14] and[15], Yamamoto, et al.[24], Belik, et al.[1], and Cliver[16]. These types of

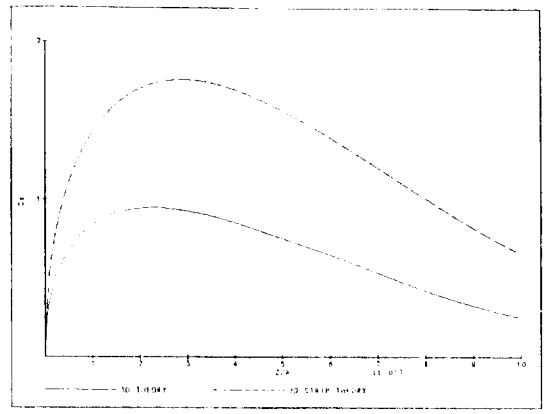

Fig. 1 Comparison between strip theory(2-D) and three dimensional theory

hydrodynamic theories assume that the ship is of sufficient length and cross sectional uniformity to allow the hull to be divided into segments, each of which is assumed to act independently of any other. A number of two-dimensional solutions are then summed to yield the total impact force. Techniques such as these are questionable in the bow region where the assumed two-dimensionality of the flow may not be valid. An illustration of the relative error of the two-dimensional approximation for three-dimensional bow loads can be seen in Figure 1. There the nondimensional impact force for a sphere, defined by $C_s=2(\text{impact force})/\rho\pi R^2V^2$, is calculated using results similar to Miloh's[12] three dimensional theory and a strip theory based upon Kaplan and Silbert's[10] or Sarpkaya and Isaacson's[18] formulas for a circular cylinder. The slam coefficient is plotted as a function of z/R, the normalized vertical distance. In both cases, the free surface is represented by an equi-potential surface and the velocity of the body is constant. While the strip theory approximation of the sphere represents an extreme example, it demonstrates the need to exercise caution when applying two-dimensional solutions in areas where three dimensional effects are large.

This paper will present the results of an investigation dealing with the three dimensional hydrodynamic impact problem. The approximate theory of von Karman[21] will be used in three dimensions

in both the vertical and horizontal planes of motion. Two different body shapes will be examined: the sphere, for comparison with previously published results and an axisymmetric flared body, similar in shape to the bow profile of a ship's forebody with large flare. The sphere will be evaluated with zero and nonzero horizontal velocity components. Both theoretical and experimental results are presented. A numerically efficient technique for the solution of the hydrodynamic three-dimensional boundary value problem will be described.

2. Problem Formulation

Consider an ideal fluid domain below the surface given by

$$z=\zeta(x,y,t) \tag{1}$$

where (x,y,z) is a right-handed coordinate system with z positive upwards and the origin located at the mean free surface. Then the complete non-linear free surface condition that the velocity potential, ϕ, must satisfy is given by(see Newman[13])

$$\frac{\partial^2\phi}{\partial t^2}+g\frac{\partial\phi}{\partial z}+2\nabla\phi\cdot\nabla\frac{\partial\phi}{\partial t}+\frac{1}{2}\nabla\phi\cdot\nabla(\nabla\phi\cdot\nabla\phi)=0 \tag{2}$$

where Eq. (2) must be true on the surface defined by Eq.(1). Following von Karman[21], we assume that when the motion of a body on the free surface occurs over a very short time interval, the temporal derivatives of the velocity potential are large compared to the spacial ones and the free surface boundary condition can be approximated as

$$\phi=0 \tag{3}$$

on $z=0$. The body boundary condition follows from

$$\frac{\partial\phi}{\partial n}=\underline{V}\cdot\underline{n} \tag{4}$$

on the instantaneous surface of the body. Here $\underline{V}$ is the velocity vector of the body with components (U,V,W) and $\underline{n}$ is the outward unit normal vector.

This boundary value problem is similar to the one proposed by von Karman[21]. It ignores effects due to changes in the local water surface elevation such as the spray jet. However, Payne[17] demonstrated that this analytical model actually prnduced results that compared better with experiments than later "improved theories", such as Wagner's splash-up factor. One possible cause for concern, though, is that this theory will not predict pressures and consequently forces on any part of the object's surface that has not passed the mean free surface. For bodies with concave shapes, such as ships with large flare, the spray sheets may contribute significantly to impact forces. In the following sections, experimental results for a flared body will be compared with theoretical calculations indicating the usefulness and limitations of this relatively simple theory.

The pressures, and subsequent forces, are found from Bernoulli's equation. Bernoulli's equation is given as

$$\frac{p}{\rho}+\frac{\partial\phi}{\partial t}+\frac{1}{2}\nabla\phi\cdot\nabla\phi+gz=\text{const} \tag{5}$$

where in a consistent theory, the quadratic term is of higher order and assumed small. The pressure may be integrated to find the forces acting on the body. In an alternative derivation, Faltinsen[5] has rederived the traditional result that the force on a body is given by

$$\text{Vertical Impact Force}=-\frac{d}{dt}(A_{33}\dot{z}_0(t))+\iint_S dS_f gzn_3 \tag{6}$$

In Eq. (6), A_{33} is the heave infinite frequency added mass coefficient as a function of submergence and $z_0(t)$ is the vertical displacement as a function of time. It is common practice to assume that the velocity of the body is constant over the time of impact. The impact force then becomes the time derivative of the added mass. By time stepping the body through the free surface, the body boundary condition can be satisfied exactly on the below-mean-waterline portion of the hull. The assumption of constant velocity is not a necessary condition but rather one of convenience. As will be demonstrated in later sections, it may be appropriate for bodies such as the sphere, but less so for the axisymmetric flared body used in this study.

Conceptually, the pressure release problem defined by Eq. (3) and (4) may be solved in a straightfor-

ward manner using distributions of surface singularities. This has been done in the field of hydrodallistics using source distributions by Wardlaw, et al.[23] for the forces acting on spheres, cones, and disks due to high-speed oblique water entry. In practice, the computational difficulties associated with three dimensional ship-like shapes and the required large number of time steps seem to have prevented researchers from actually using this method to calculate forces for arbitrary bodies. Oliver[16] gives one example of large computer time estimates for solving extreme ship motion problems.

In this work, the hydrodynamic boundary value problem at each time step will be solved using a normal dipole distribution with a corresponding interior flow. This technique is an expansion of that outlined by Chang and Pien[3] and Yeung[25]. In particular, from the classical use of Green's theorem the dipole strength is equal to the difference between the interior and exterior potentials. Solving for the dipole strength with a known interior flow immediately yields the exterior potential and thus the pressures. Breslin, et al.[2] has shown that the interior problem is equivalent to the interior fluid moving vertically as a solid mass of water. For horizontal motion, it will be demonstrated in the following paragraphs that the interior problem is represented by a dipole sheet on the inner free surface with the interior fluid mass moving horizontally.

3. Problem Solution

Consider a body with bounding surfaces and outward unit normal n as shown in Fig. 2. The exterior and interior domains are R_e and R_i respectively. The exterior bounding surfaces on the free surface, body, and at infinity are given as S_{Fe}, S_B, and S_∞. The interior bounding surfaces are the interior free surface, S_{Fi}, and the body, S_B. The usual governing equations for the velocity potential, $\phi(X)$, and a Green function $G(X;Y)$, are

$$\nabla^2\phi(X) = 0$$
$$-\nabla^2 G(X;Y) = \delta(X-Y) \tag{7}$$

where X is the vector to the field point, Y is the vector to the source point, and $\delta(X-Y)$ is the Dirac delta function. Through the application of Green's second identity in R_e the exterior potential is given as

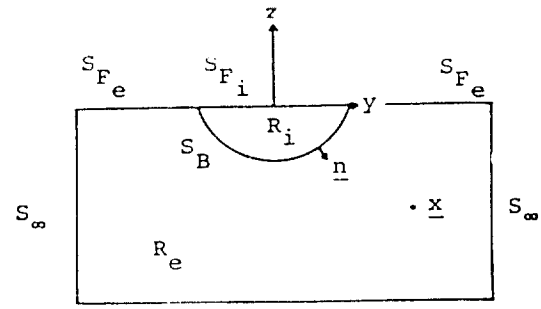

Fig. 2 Coordinate system and bounding surfaces

$$\phi_e(X) = -\iint_{S_B+S_{Fe}+S_\infty} \left\{ G(X;Y)\frac{\partial\phi_e(Y)}{\partial n} - \phi_e(Y)\frac{\partial G(X;Y)}{\partial n} \right\} dS \tag{8}$$

When Green's second identity is applied again in R_i, the result is

$$-\iint_{S_B+S_{Fi}} \left\{ G(X;Y)\frac{\partial\phi_i(Y)}{\partial n} - \phi_i(Y)\frac{\partial G(X;Y)}{\partial n} \right\} dS = 0 \tag{9}$$

Subtracting Eq. (9) from Eq. (8) gives

$$\begin{aligned}\phi_e(X) = &-\iint_{S_B} \left\{ G(X;Y)\left(\frac{\partial\phi_e(Y)}{\partial n} - \frac{\partial\phi_i(Y)}{\partial n}\right) - (\phi_e(Y)-\phi_i(Y))\frac{\partial G(X;Y)}{\partial n} \right\} dS \\ &-\iint_{S_{Fe}} \left\{ G(X;Y)\frac{\partial\phi_e(Y)}{\partial n} - \phi_e(Y)\frac{\partial G(X;Y)}{\partial n} \right\} dS \\ &+\iint_{S_{Fi}} \left\{ G(X;Y)\frac{\partial\phi_i(Y)}{\partial n} - \phi_i(Y)\frac{\partial G(X;Y)}{\partial n} \right\} dS \\ &-\iint_{S_\infty} \left\{ G(X;Y)\frac{\partial\phi_e(Y)}{\partial n} - \phi_e(Y)\frac{\partial G(X;Y)}{\partial n} \right\} dS \end{aligned} \tag{10}$$

For the pressure release problem, the appropriate Green function is

$$G(X;Y) = \frac{1}{4\pi}\left(\frac{1}{|X-Y|} - \frac{1}{|X-Y'|}\right) \tag{11}$$

where Y' is an image vector of Y about $z=0$. Since both $G(X;Y)$ and $\phi_e(X)$ are zero on S_{Fe} and far

from the body both go to zero at a sufficient rate, the integrals S_∞ and S_{Fe} contribute nothing in Eq. (10). The interior potential is arbitrary and selected such that the normal derivatives of the interior and exterior problems are continuous. In other words,

$$\frac{\partial \phi_e}{\partial n} - \frac{\partial \phi_i}{\partial n} = 0 \quad \text{on } S_B.$$

The resulting surface dipole distribution has a strength defined as μ where $\mu = \phi_i - \phi_e$ on S_B. From Eq. (10), the following form for the exterior potential is

$$\phi_e(\underline{X}) = -\iint_{S_B} \mu(\underline{Y}) \frac{\partial G(\underline{X};\underline{Y})}{\partial n} dS + \iint_{S_{Fi}} \left\{ G(\underline{X};\underline{Y}) \frac{\partial \phi_i(\underline{Y})}{\partial n} - \phi_i(\underline{Y}) \frac{\partial G(\underline{X};\underline{Y})}{\partial n} \right\} dS \tag{12}$$

As $\underline{X}$ approaches a boundary point on the surface S_B, the exterior potential becomes

$$\phi_e(\underline{X}) = -\frac{\mu(\underline{X})}{2} - \iint_{S_B} \mu(\underline{Y}) \frac{\partial G(\underline{X};\underline{Y})}{\partial n} dS + \iint_{S_{Fi}} \left\{ G(\underline{X};\underline{Y}) \frac{\partial \phi_i(\underline{Y})}{\partial n} - \phi_i(\underline{Y}) \frac{\partial G(\underline{X};\underline{Y})}{\partial n} \right\} dS \tag{13}$$

for $\underline{X}$ on S_B. Since $\phi_e(\underline{X}) = \phi_i(\underline{X}) - \mu(\underline{X})$ on S_B, the above equation becomes

$$\phi_i(\underline{X}) = \frac{\mu(\underline{X})}{2} - \iint_{S_B} \mu(\underline{Y}) \frac{\partial G(\underline{X};\underline{Y})}{\partial n} dS + \iint_{S_{Fi}} \left\{ G(\underline{X};\underline{Y}) \frac{\partial \phi_i(\underline{Y})}{\partial n} - \phi_i(\underline{Y}) \frac{\partial G(\underline{X};\underline{Y})}{\partial n} \right\} dS \tag{14}$$

which is a Fredholm integral equation of the second kind.

3.1. Determination of the Interior Potentials

The governing equation for the interior potential, ϕ_i, in R_i is the Laplace equation. On the body surface, S_B, the boundary condition for ϕ_i is

$$\frac{\partial \phi_i}{\partial n} = \frac{\partial \phi_e}{\partial n} = \underline{V} \cdot \underline{n}.$$

By also setting

$$\frac{\partial \phi_i}{\partial n} = \underline{V} \cdot \underline{n}$$

on the interior free surface, S_{Fi}, ϕ_i is determined uniquely in R_i except for an arbitrary constant. The special cases of rigid body motion in heave and sway are discussed below.

For heave, let the interior potential be given as

$$\phi_i(\underline{X}) = Wz \tag{15}$$

where W is the vertical velocity component and $\underline{X}$ is in R_i. By inspection, it is clear that the condition of

$$\frac{\partial \phi_i}{\partial n} = \underline{V} \cdot \underline{n}$$

is satisfied on both S_B and S_{Fi}. Since both $\phi_i(\underline{X}) = 0$ and $G(\underline{X};\underline{Y}) = 0$ on S_{Fi}, Eq. (14) becomes

$$\phi_i(\underline{X}) = \frac{\mu(\underline{X})}{2} - \iint_{S_B} \mu(\underline{Y}) \frac{\partial G(\underline{X};\underline{Y})}{\partial n} dS \tag{16}$$

for $\underline{X}$ on S_B.

For sway, let the interior potential be given as

$$\phi_i(\underline{X}) = Vy \tag{17}$$

where V is the horizontal velocity component and $\underline{X}$ is in R_i. Again by inspection, it is clear that the condition of

$$\frac{\partial \phi_i}{\partial n} = \underline{V} \cdot \underline{n}$$

is satisfied on both S_B and S_{Fi}. The integral equation in this case is somewhat more complex than for heave since ϕ_i is not zero on S_{Fi}. Using the fact that $G(\underline{X};\underline{Y}) = 0$ on S_{Fi}, or alternatively that

$$\frac{\partial \phi_i}{\partial n} = 0$$

on S_{Fi}, Eq. (14) becomes

$$\phi_i(\underline{X}) + \iint_{S_{Fi}} (V\eta) \frac{\partial G(\underline{X};\underline{Y})}{\partial n} dS = \frac{\mu(\underline{X})}{2} - \iint_{S_B} \mu(\underline{Y}) \frac{\partial G(\underline{X};\underline{Y})}{\partial n} dS \tag{18}$$

for $\underline{X}$ on S_B.

The dipole strengths for the heave and sway problems are given as the solutions to Eq. (16) and Eq. (18) respectively. With these strengths known and the interior potential given, the relation may be used to find the exterior potentials. This method of solving boundary value problems eliminates the need to find the values of the Green function.

3.2. Determination of the Impact Pressures

Once the potential is known, the pressures may be found by applying Eq.(5), Bernoulli's Equation. Bernoulli's equation is derived for variables relative to an inertial coordinate system. However, it is convenient for the purpose of solving the impact

boundary value problem to use body fixed coordinates. Under these circumstances, spacial differentiation is invariant with coordinate transformation, but temporal differentiation is not. If $\underline{X}$ is a position vector in the inertial coordinates and $\underline{X}'$ is a position vector in the body fixed coordinates, then they are related by

$$\underline{X}'=\underline{X}-\int_0^t \underline{V}(t)dt \tag{19}$$

where $\underline{V}(U, V, W)$ is the velocity vector of the body and

$$\frac{\partial x'}{\partial t}=-U(t),\quad \frac{\partial y'}{\partial t}=-V(t),\quad \frac{\partial z'}{\partial t}=-W(t). \tag{20}$$

Let $\phi(\underline{X}, t)$ be the potential in inertial coordinates and $\phi'(\underline{X}, t)$ the potential in body fixed coordinates, then by virtue of the chain rule of calculus

$$\frac{\partial \phi_e(\underline{X}, t)}{\partial t}=\frac{\partial \phi_e'(\underline{X}', t)}{\partial t}-U(t)\frac{\partial \phi_e'(\underline{X}', t)}{\partial x'} -V(t)\frac{\partial \phi_e(\underline{X}', t)}{\partial y'}-W(t)\frac{\partial \phi_e'(\underline{X}', t)}{\partial z'} \tag{21}$$

Bernoulli's Equation, then, in body fixed coordinates is

$$\frac{p(\underline{X}', t)}{\rho}=-\Big\{\frac{\partial \phi_e'(\underline{X}', t)}{\partial t} -\Big(U(t)\frac{\partial \phi_e'(\underline{X}', t)}{\partial x'}+V(t)\frac{\partial \phi_e'(\underline{X}', t)}{\partial y'} +W(t)\frac{\partial \phi_e'(\underline{X}', t)}{\partial z'}\Big) +\frac{1}{2}\nabla\phi_e'(\underline{X}', t)\cdot\nabla\phi_e'(\underline{X}', t)+gz\Big\} \tag{22}$$

Integrating $\frac{\partial \phi_e'}{\partial t}n_3$ over the body, where n_3 is the vertical component of the unit normal, yields the time derivative of the added mass as discussed previously. The force resulting from the convective terms in Eq. (22) does not appear in the traditional calculations. (See Eq. (6)). The influence of the various force components are discussed in later sections. The time differential in Eq. (22) is found through numerical differentiation of the potential at various time steps. The fluid velocity vector in body fixed coordinates, $\nabla(\phi_e')$, with components (u, v, w) is found by using the vortex lattice concept. Following Thrasher [20] and others, the jump in velocity vector, $\underline{V}_e-\underline{V}_i$, across a normal dipole sheet can be represented by the vector cross product between the unit surface normal, $\underline{n}$, and the vorticity vector, $\underline{\omega}$, or

$$\underline{V}_e=\underline{V}_i-\underline{n}\times\underline{\omega} \tag{23}$$

Here $\underline{V}_e$ and $\underline{V}_i$ are the surface velocity vectors on the exterior and interior surfaces respectively. The numerical determination of the vorticity vector is described in the next section.

Given the pressures by Eq. (22), the forces and consequently the accelerations may be found through integration. The usual relations for the accelerations, velocities, and displacements are shown below.

$$F_z=m\ddot{Z}=-\iint pn_z dS$$

$$F_y=m\ddot{Y}=-\iint pn_y dS \tag{24}$$

$$\dot{Z}(t)=\int_0^t \ddot{Z}(t)dt \qquad \dot{Y}(t)=\int_0^t \ddot{Y}(t)dt$$

$$Z(t)=\int_0^t \dot{Z}(t)dt \qquad Y(t)=\int_0^t \dot{Y}(t)dt \tag{25}$$

3.3. Computational Details

The surface description of the body and the solutions to the integral equations, Eqs. (16) and (18), follow the method of Hess and Smith [8]. In the interest of computational efficiency, the body was divided vertically into four or five large blocks. The boundary value problems were solved and the velocity potential and velocity vector on the body were calculated in 8~10 time steps for each block. For the particular examples used in this paper, symmetry reduced the number of elements by a factor of four. In any particular block, the number of circumferential elements, M, was fixed and the number of vertical (azimuthal) elements was increased by one for each time step. Thus, at time t_1 the number of elements was MN and at time $t_1+\Delta t$ the number was $M(N+1)$. For the examples considered in this paper, the range of N was 8 to 16 and the range of M was 6 to 8. When elements were required on the inner free surface, as in the sway problem, the number of surface elements was $(M-1)$. The velocity potential for body fixed coordinates was assumed to locally follow a second order polynomial with respect to time. The partial derivative was easily found as shown below

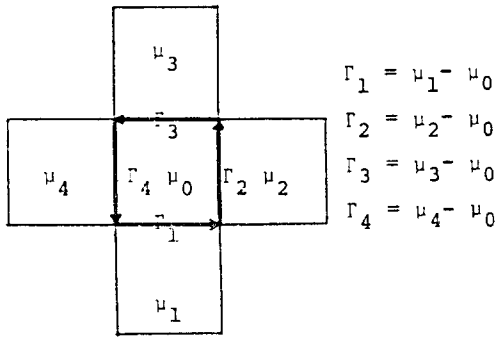

Fig. 3 Determination of vortex filaments from normal dipole surface distributions

$$\frac{\partial \phi_e'(\underline{X}', t_1)}{\partial t} = \frac{t_1 - t_2}{(t_0 - t_2)(t_0 - t_1)} \phi_e'(\underline{X}', t_0) + \frac{2t_1 - t_2 - t_0}{(t_1 - t_2)(t_1 - t_0)} \phi_e'(\underline{X}', t_1) + \frac{t_1 - t_0}{(t_2 - t_1)(t_2 - t_0)} \phi_e'(\underline{X}', t_2) \quad (26)$$

The vorticity vector, $\underline{\omega}$, used in the determination of the velocity vector $\underline{V}_e$, is found using the vortex lattice method(Thrasher[20]). Since the doublet strength is assumed to be constant over a panel, the local induced velocity is equivalent to the line integral of the vortex filament strengths. As shown in Figure 3, the net vortex strength is found by superimposing adjacent elements. The vorticity vector at the j-th panel null point, $\underline{\omega}_j$, is given by

$$\underline{\omega}_j = \sum_{i=1}^{m} \frac{\underline{l}_i \Gamma_i}{A_j + A_i} \quad (27)$$

where $\underline{l}_i$ denotes the vectors connecting consecutive nodes of the j-th panel, Γ_i is the branch circulation of the corresponding vortex segments, A_j is the area of the j-th panel, A_i is the area of the adjoining panel on the i-th side, and m is the number of panel edges, either three or four.

The velocity at the free surface ($z=0$) in the idealized double body problem is infinite for non-wallsided shapes. Numerically this is represented by large values for the vortex strengths on the panels next to that equi-potential surface. Based upon the physics of the problem, and the two dimensional results for the pressure distribution in the spray jet (see Yim[26], Gallagher and McGregor [6], and Greenhow [7]), the vortex strengths for filaments at the free surface were equated to the lower adjacent ones.

The computer program was verified by comparing results with the works of Miloh [12] and Hulme [9]. For the later, a 20×20 segmented quarter hemisphere gave a result that was within 0.9% of the published value for the sway added mass coefficient(0.2732) and within 0.2% for the heave added mass coefficient(0.500).

4. Theoretical and Experimental Comparisons

Impact experiments were conducted in the Ship Hydrodynamics Laboratory at the University of Michigan. As mentioned in the introduction of this paper, two different body shapes were tested: a sphere, and an axisymmetric flared body, similar in shape to the bow profile of a ship's forebody with large flare.

The sphere was a composite construction of plexiglass, concrete, wood and metal. It was ballasted to float as a hemisphere. The outside diameter was 0.502m (19.8in). The flared body was of similar construction. Both the sphere and flared body dimensions and profiles are shown in Figure 4. Also shown are the panel distributions used in the computations. The flared body had a total weight of 74.7N (16.8 lbs) and floated at approximately 90% of the total height of the body. A transferable instrument packet containing two accelerometers, one for vertical acceleration and one for horizontal acceleration, was used in both bodies. With these measurements the time history of the impact force can be easily determined since the force is equal to the mass of the object multiplied by the instantaneous acceleration. The accelerometers were of the piezoelectric type with a natural frequency in excess of 35K Hz.

The test matrix included dropping the sphere and flared body from three heights, 0.61m(2 ft), 1.22m (4 ft), and 1.83m (6 ft). These corresponded to impact velocities of 3.46m/s (11.3 ft/s), 4.89m/s (16.0 ft/s), and 5.99m/s (19.7 ft/s) respectively. For the 0.61m (2 ft) and 1.22m (4 ft) heights, the

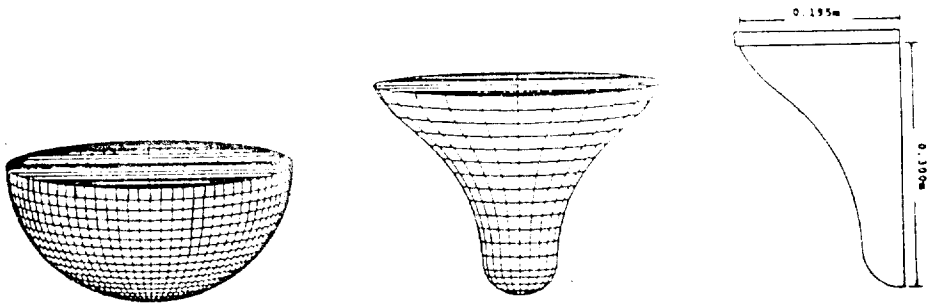

Fig. 4 Sphere and flared body panel distributions and dimensions.

sphere was also dropped from a moving carriage with a speed that corresponded to the vertical impact velocity. This resulted in an oblique entry angle of 45 degrees. Each drop was performed two or three times as a check on repeatability. The level of repeatability was good as discussed in the Appendix A1.

4.1. Experimental Results

Both the dimensional and non-dimensional results are displayed in the following figures. Figures 5 and 6 show the dimensional acceleration in multiples of the gravitational constant plotted as a function of elapsed time in milliseconds. They show the vertical acceleration for the sphere and flared body with zero horizontal velocity respectively. All three drop heights are included.

The dimensional results of Figures 5 and 6 are replotted in nondimensional form in Figures 7 and 8. Figure 9 is a plot of nondimensional vertical and

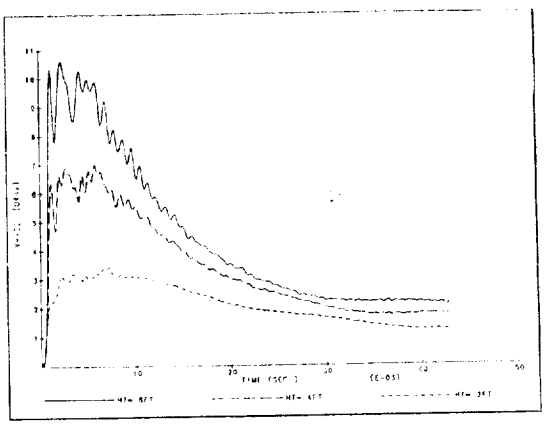

Fig. 5 Experimental impact accelerations for a sphere(dimensional)-three drop heights

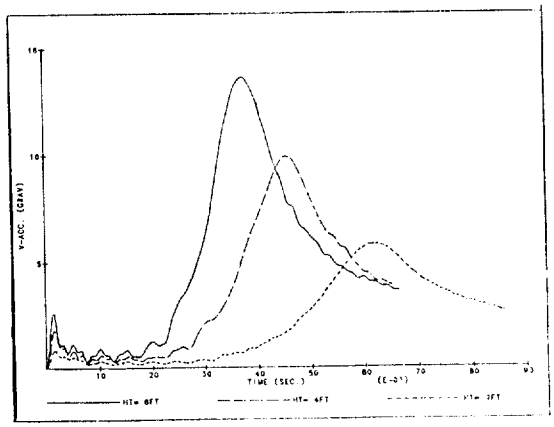

Fig. 6 Experimental impact accelerations for a flared body(dimensional)-three drop heights

horizontal accelerations for the sphere with a 45 degree entrance angle. Both drop heights for this case are included. The vertical slamming coefficient, C_{vs}, replaces the vertical acceleration. It is defined as

$$C_{vs}=\frac{2m\ddot{Z}}{\rho\pi L^2 V_0^2} \tag{28}$$

where m is the mass, $\ddot{Z}$ is the vertical acceleration, ρ is the water density, L is some representative length, (the radius for the sphere and half the top transverse dimension for the flared body, 0.195m (7.7 in), $D=2L$ and V_0 is the initial vertical impact velocity. The time axis has been normalized by D/V_0. For oblique entry impact, the horizontal slamming coefficient, C_{hs}, is defined. In it, the horizontal acceleration, $\dot{Y}$, replaces the vertical acceleration.

In the non-dimensional plots for the sphere(Figure 7), the normalized accelerations have approximately

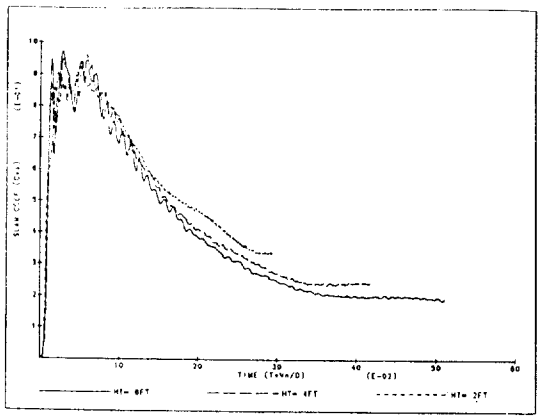

Fig. 7 Experimental nondimensional vertical slam coefficients for a sphere-three drop heights

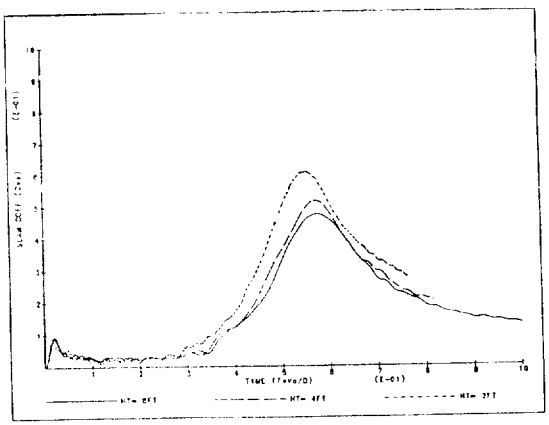

Fig. 8 Experimental nondimensional vertical slam coefficients for a flared body-three drop heights

the same maximum value. However, the normalized maximum impact for the flared body (Figure 8) is dependent on the drop height. As time or the depth of immersion increase, the buoyancy becomes relatively more significant for bodies dropped from lower heights. Also, if the body accelerates and the velocity fails to remain constant, then the normalization is not completely valid. This is consistent with Eq. (22), Bernoulli's equation, where the velocity potential terms for constant velocity may be normalized by the velocity squared, but the hydrostatic term, gz, follows the Froude scaling law.

The non-dimensional maximum vertical impact

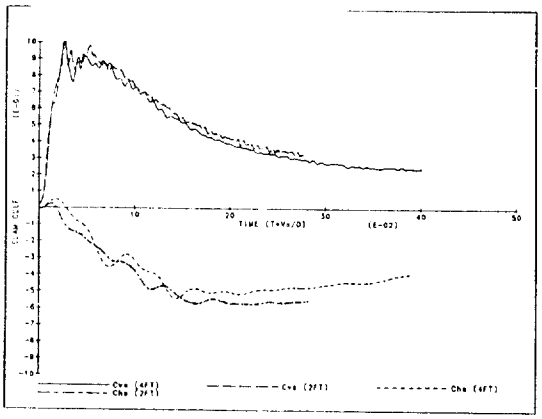

Fig. 9 Experimental nondimensional vertical and horizontal slam coefficients for a sphere-two drop heights

force for the oblique entry test (Fig. 9) does not differ significantly from the normal entry results. This indicates that the coupling force for the sphere (the vertical force due to horizontal impact velocity) is not large. The maximum of the horizontal force is somewhat smaller relative to that of the vertical force and occurs at a latter time. The above conclusions are clearly hull-form dependent and would not necessarily hold for long, slender shapes experiencing oblique slamming.

4.2. Theoretical Results

The effect of the buoyancy terms is shown in Fig. 10 and 11 for the sphere and flared body respectively. Constant velocity during the entire

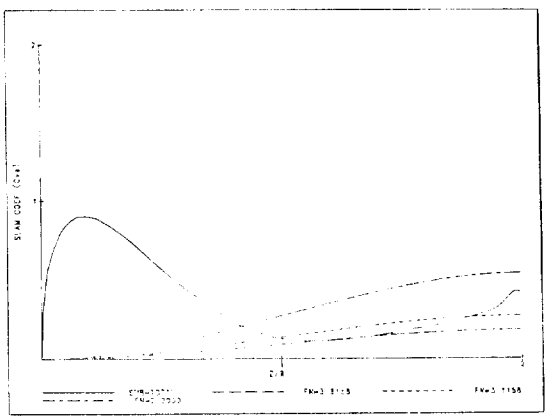

Fig. 10 Effect of buoyancy in the vertical impact force of a sphere-three drop froude nos

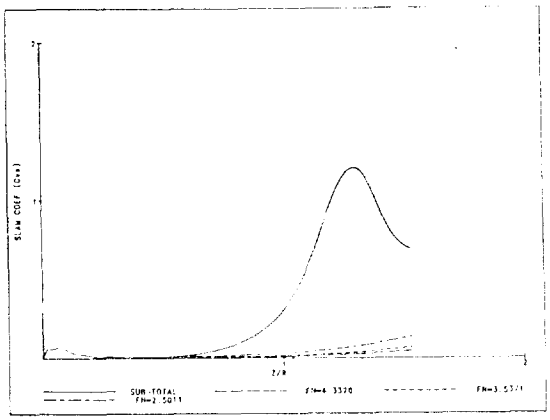

Fig. 11 Effect of buoyancy in the vertical impact force of a flared body-three drop froude nos

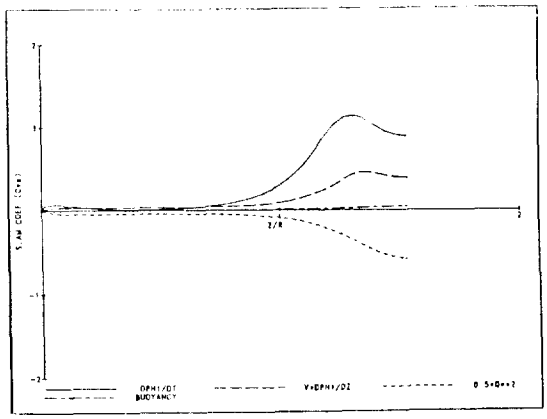

Fig. 13 Various force components acting on a flared body during vertical impact (FN=4.3320)

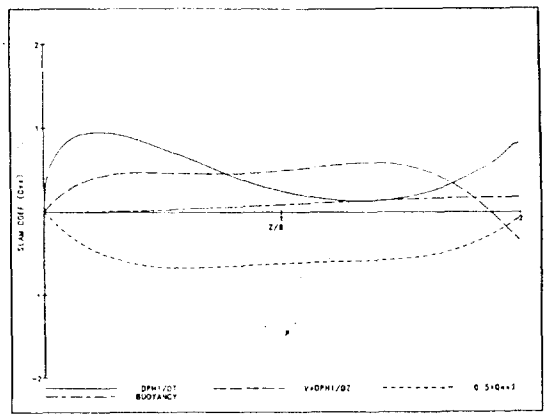

Fig. 12 Various force components acting on a sphere during vertical impact (FN=3.8158)

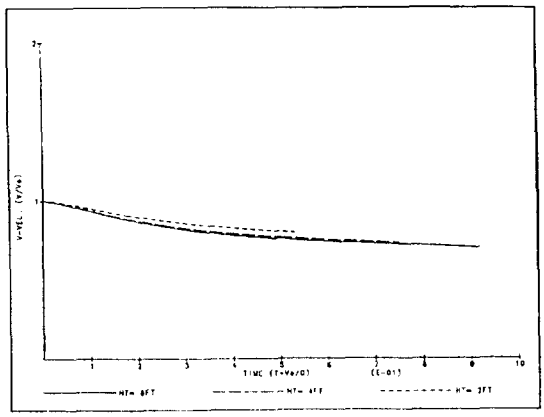

Fig. 14 Time simulation of the vertical velocity of a sphere dropped from various heights (FN=2.2030, 3.1156, 3.8158)

immersion was assumed. The hydrostatic term has been separated from the rest of the theoretical pressure terms in Eq. (22). The velocity potential contributions were integrated and plotted as the solid line, labeled SUBTOTAL. The normalized buoyancy forces for three different drop Froude Numbers are shown as the dashed lines. The drop Froude Number is defined as $V_0/\sqrt{gL}$ where V_0 and L are defined in Eq. (28). All the force components were normalized by the factors $0.5\rho\pi L^2 V_0^2$, consistent with Eq. (28). Similar to the experimental terms normalized with respect to the velocity squared become relatively more important for the impact forces with lower inital velocities.

The various force components of the different pressure terms in Eq. (22) are shown in Fig. 12 and 13 for the sphere and flared body respectively. Initial velocities corresponding to drop Froud Numbers of 3.8158 for the sphere and 4.3320 for the cusp were assumed. These velocities remained constant during the impact fall. It is of interest to note that numerically, the term associated with the coordinate transformation of the time derivative, V*DPHI/DZ (see Eq. (21)), approximately cancels the quadratic velocity term, $0.5*Q^2$. The solid line in Fig. 12, representing the time derivative of the velocity

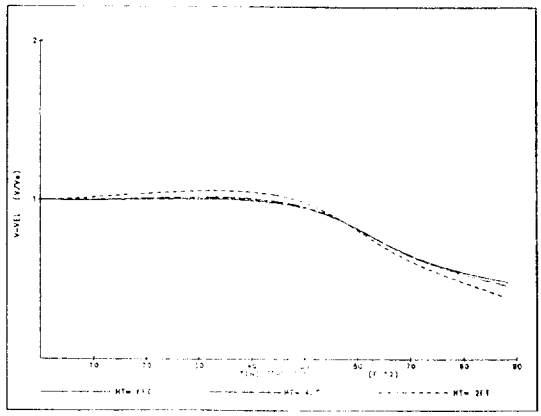

Fig. 15 Time simulation of the vertical velocity of a flared body dropped from various heights (FN=2.5011, 3.5371, 4.3320)

potential in body fixed coordinates, has a maximum of $C_{vs}\approx 0.952$. This value compares well with the results published by Miloh[12] where an equation analogous to Eq. (6) was used to find the vertical slam coefficient. The maximum value of the slam coefficient for a sphere including all the terms of Eq. (22) except buoyancy, is $C_{vs}\approx 0.903$. See Fig. 10.

Simulations of the velocity time histories for the two bodies are shown in Fig. 14 and 15. Three different drop heights corresponding to drop Froude Numbers of 2.2030, 3.1156, and 3.8158 for the sphere and 2.5011, 3.5371, and 4.3320 for the flared body are displayed. The instantaneous velocity has been normalized by the initial impact velocity. For each time step, the forces, accelerations, velocities, and displacements were calculated using Eqs. (24) and (25). Clearly, the velocities do not remain constant during the fall. The maximum impact force for the sphere occurs at a non-dimensional time (TV_0/D) of 0.062, a point where the velocity has been reduced by approximately 5.0%. For the flared body, the maximum is at $TV_0/D=0.63$ and the velocity has been reduced by 23.1%. These curves suggest that impact calculations should include the acceleration and velocity changes due to body dynamics. This is particularly true for flared bodies where the location of maximum force corresponds to a significant decrease in velocity.

4.3. Comparison Between Theory and Experiment

A comparison of the theoretical and experimental non-dimensional results are shown in Figs. 16, 17, and 18. In Fig. 16, the sphere test results with a perpendicular entrance angle are given for the three different drop heights. Fig. 17 shows the flared body results for similar conditions. The sphere test results with the 45 degree oblique entrance angle are shown in Fig. 18 for two drop heights. velocities used in the theoretical calculations varied in time as described in the previous section. The theoretical maximum slam coefficients in Fig. 16~18 differ from the ones in Fig. 10 and 11 due to the decrease in velocities and the addition of the buoyancy terms.

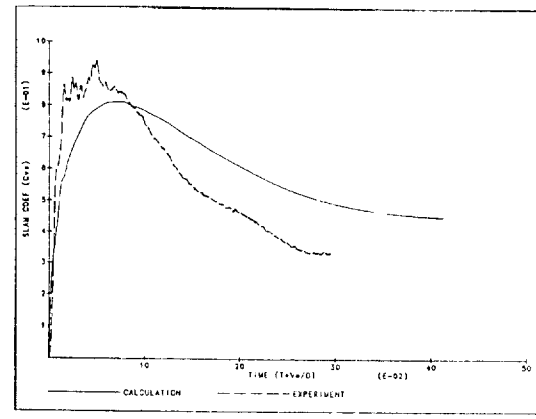

Fig. 16a Comparison between theory and experiment of the vertical slam coefficient for a sphere(FN=2.2030)

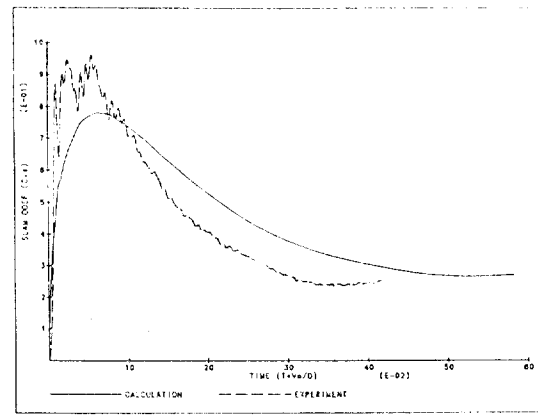

Fig. 16b Comparison between theory and experiment of the vertical slam coefficient for a sphere(FN=3.1156).

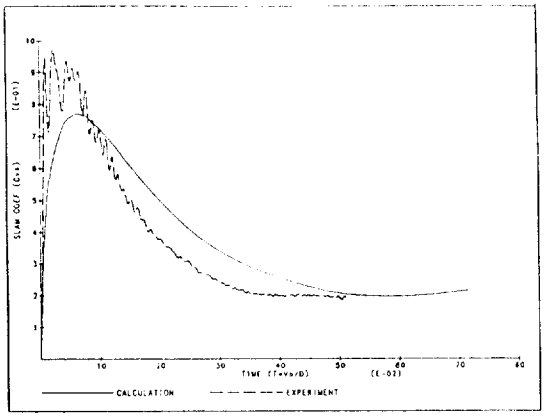

Fig. 16c Comparison between theory and experiment of the vertical slam coefficient for a sphere(FN=3.8158)

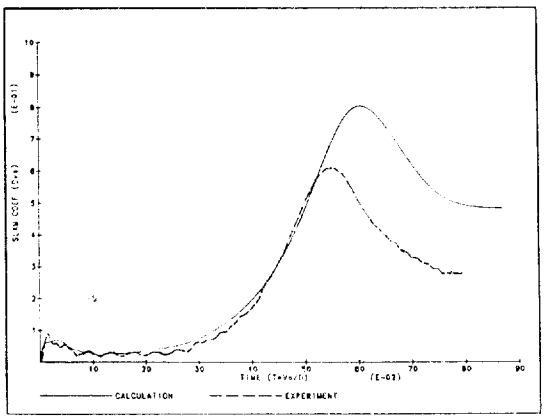

Fig. 17a Comparison between theory and experiment of the vertical slam coefficient for a flared body(FN=2.5011)

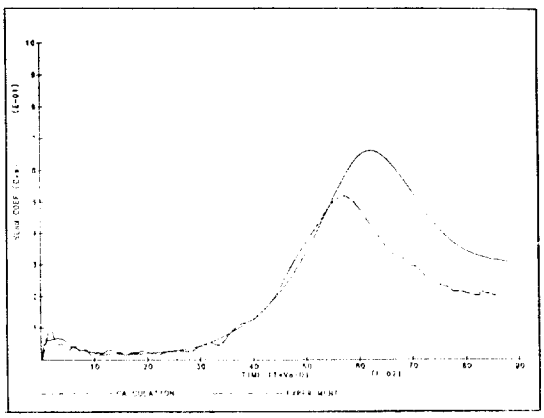

Fig. 17b Comparison between theory and experiment of the vertical slam coefficient for a flared body(FN=3.5371)

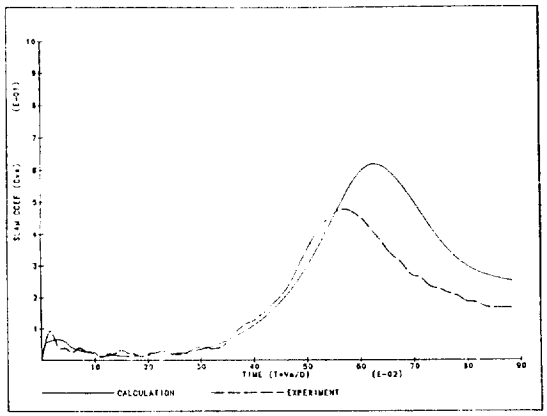

Fig. 17c Comparison between theory and experiment of the vertical slam coefficient for a flared body(FN=4.3320)

Generally, the theory seems to under predict the maximum vertical impact force for the sphere by approximately 5 to 10%. Conversely, the theory over predicts the maximum vertical force of the flared body. This is possibly a result of the spray jet separating from the flared upper sections. The theory also tends to stretch the duration of the impact out when compared with experiment. This is true for both the sphrere and flared body.

The theoretical horizontal slam coefficient, C_{hs}, does not predict the sharp rise in impact force. While it approaches the same maximum value, it does so at a much later time. The experimental

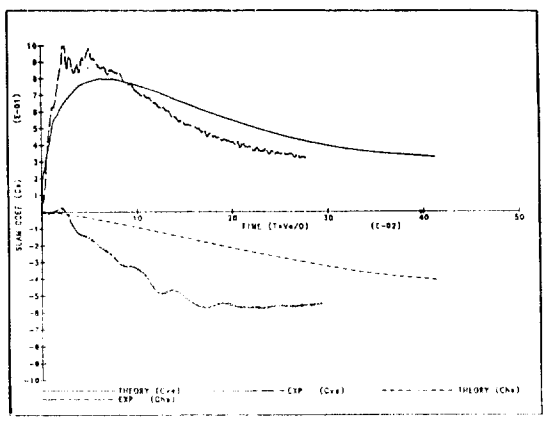

Fig. 18a Comparison between theory and experiment of the vertical and horizontal slam coefficients for a sphere at an oblique angle of impact(FN=2.2030)

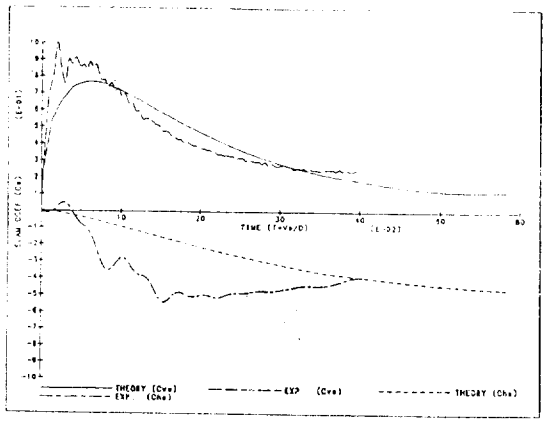

Fig. 18b Comparison between theory and experiment of the vertical and horizontal slam coefficients for a sphere at an oblique angle of impact(FN=3.1156)

results may be due to the sphere impacting on the water in the forward spray sheet. This, of course, is not contained in the theoretical model.

5. Summary and Conclusions

The three dimensional characteristics of the impact problem have been discussed. Two different hull shapes, a sphere and a flared body, were evaluated for impact forces. Theoretical and experimental comparisons were made. The the theoretical calculations were done using dipole distributions with a known interior flow and an equi-potential free surface condition. The addition of the interior flow reduced the computation time significantly. The contributions from the various terms in Bernoulli's equation were described. Theory under predicted the maximum force of the sphere but over predicted the force for the flared body. The presence of the spray jet, which was not included in the theory, may be important in attenuating the maximum impact force in flared bodies.

Acknowledgment

This work was supported by the Maritime Administration University Research Program, contract DTM91-83-C-50118 and the Department of Naval Architecture and Marine Engineering, The University of Michigan. Acknowledgement is also given to the Korea Research Institute of Ships and Ocean Engineering(KRISO).

References

[1] Belik, O., Bishop, R.E.D. and Price, W.G., "A Simulation of Ship Responses Due to Slamming in Irregular Head Seas", *RINA*, Vol. 124, 1982.

[2] Breslin, J. et al., "Theoretical and Experimental Propeller-Induced Pressures Arising from Intermittent Blade Cavitation, Loading, and Thickness", *SNAME Transactions*, Vol. 90, 1982.

[3] Chang, M.S. and Pien, P.C., "Hydrodynamic Forces on a Body Moving Beneath a Free Surface", 1st International Conference on Numerical Ship Hydrodynamics, National Bureau of Standards, Gaithersburg, Maryland, pp. 539-559, 1975.

[4] Chuang, S.L., "Theoretical Investigations on Slamming of Cone-Shaped Bodies", *Journal of Ship Research*, Vol. 13, No. 4, 1969.

[5] Faltinsen, O., "Numerical Solution of Transient Nonlinear Free-Surface Motion Outside or Inside Moving Bodies", Second International Conference on Numerical Ship Hydrodynamics, University of California, Berkeley, California, 1977.

[6] Gallagher, P. and McGregor, R.C., "Slamming Simulations: An Application of Computational Fluid Dynamics", Fourth International Conference on Numerical Ship Hydrodynamics, Washington, D.C, 1985.

[7] Greenhow, M., "Wedge Entry into Initially Calm Water", Marintek, Report No. OR 530030. 12, Trondheim, Norway, 1986.

[8] Hess, J.L. and Smith, H.M.O., "Calculation of Potential Flow About Arbitrary Bodies", Progress in Aeronautical Sciences, Vol. 8, pp. 1-138, Pergamon Press, New York, New York, 1967.

[9] Hulme, A., "The Wave Forces Acting on a Floating Hemisphere Undergoing Forced Periodic Cscillations", *Journal of Fluid Mechanics*, Vol. 121, pp. 443-463, 1982.

[10] Kaplan, P. and Silbert, M.N., "Impact Forces on Platform Horizontal Members in the Splash Zone", OTC Paper No. 2498, Houston, TX, 1976.

[11] Kaplan, W., *Operational Methods for Linear Systems*, Addison-Wesley, Reading, Massachusetts, 1962.

[12] Miloh, T., "Wave Slam on a Sphere Penetrating a Free Surface", *Journal of Engineering Math.*, Vol. 15, No. 3, pp. 221-240, 1981.

[13] Newman, J.N., *Marine Hydrodynamics*, MIT Press, Cambridge, Massachusetts, 1977.

[14] Cchi, M.K. and Motter, L.E., "Prediction of Extreme Values of Impact Pressure Associated with Ship Slamming", *Journal of Ship Res.*, Vol. 13, No. 2, 1969.

[15] Cchi, M.K. and Motter, L.E., "Prediction of Slamming Characteristics and Hull Responses for Ship Design", *SNAME Transactions*, pp. 144-176, 1973.

[16] Oliver, J.C., "Advanced Method for Ship Motion and Wave-Load Predictions", Ship Structure Committee Project, SR 1277, Giannotti and Assoc., Annapolis, Maryland, 1983.

[17] Payne, P.R., "The Vertical Impact of a Wedge on a Fluid", Ccean Engineering, Vol. 8, No. 4, pp. 421-436, 1981.

[18] Sarpkaya, T. and Isaacson, M., *Mechanics of Wave Forces on Offshore Structures*, Van Nostrand Reinhold Co., New York, New York, 1981.

[19] Shiffman, M. and Spencer, D.C., "The Force of Impact on a Cone Striking a Water Surface", Comm. Pure Appl. Math., Vol. 4, pp. 379-417, 1951.

[20] Thrasher, D.F., "Application of the Vortex-Lattice Concept to Flows with Smooth-Surface Separation", Fourteenth Symposium on Naval Hydrodynamics, The University of Michigan, Ann Arbor, Michigan, pp. 1089-1113, 1983.

[21] von Karman, T., "The Impact on Seaplane Floats During Landing", NACATN 321, 1929.

[22] Wagner, H., "Landing of Seaplanes", NACATN 62, 1931.

[23] Wardlaw, A.B., Morrison, A.M., and Baldwin, J.L., "Prediction of Impact Pressures, Forces, and Moments During Vertical and Oblique Water Entry", Naval Surface Weapons Center, White Oaks Laboratoratories NSWC/WOL/TR 77-16, 1977.

[24] Yamamoto, Y., Fujino, M., and Fukasawa, T., "Motion and Longitudinal Strength of a Ship in Head Seas and the Effects of Nonlinearities", Naval Architecture and Ocean Engineering, Vol. 18, Soc. of Nav. Arch. of JAPAN, 1980.

[25] Yeung, R., "Numerical Methods in Free Surface Flows", Ann. Rev. Fluid Mech., Vol. 14, pp. 395-442, 1982.

[26] Yim, B., "Numerical Solution for Two-Dimensional Wedge Slamming With a Nonlinear Free-Surface Condition", Fourth International Conference on Numerical Ship Hydrodynamics, Washington, D.C., 1985.

[27] Yung, T.-W., by personal communication, 1982.

Appendix A1 Experiments

The experiments which were conducted at the Ship Hydrodynamics Laboratory(SHL) investigated both vertical and oblique angles of impact. For the vertical tests, two shapes(a sphere and a flared body) were dropped from three heights. For the oblique impact tests, the sphere was dropped from SHL towing carriage. The carriage speed matched the vertical component of the initial impact velocity resulting in an oblique entrance angle of 45 degrees.

The vertical accelerations were measured for the vertical impact tests while the vertical and horizontal accelerations were measured for the oblique tests. The accelerometer transducers(PCB Piezotronics Inc., model no. 302A02) had natural frequencies exceeding 35KHz. An instrument package was constructed to expedite the transfer of the accelerometers between the sphere and flared body. This package could be

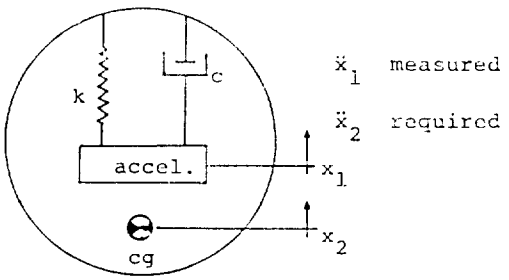

Fig. A1 Dynamic model of the experimental apparatus

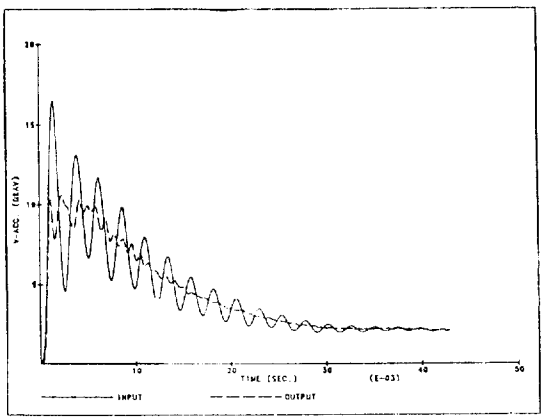

Fig. A2 Experimental impact time history-measured transducer acceleration (input) and acceleration of body. center of gravity(output)

bolted into the top of either shape and the whole assembly made watertight.

Analog signals from the accelerometers were digitized at a sampling rate of 21KHz. Due to the flexibility of the sphere or flared body, the total system natural frequency was considerably lower than the natural frequency of the individual transducers. Natural frequencies of approximately 450Hz and 275Hz were estimated for the sphere and flared bodies respectively. These frequencies resulted in adequate rise times for the lower drop heights where the initial velocities were relatively small and the duration of impact stretched out. However, at the higher drop heights, the steep rise time produced significant dynamic system response increasing the measured maximum acceleration.

In order to get the acceleration of the center of gravity of the impact body from an accelerometer suspended inside that body, the entire system was modeled as a single degree-of-freedom spring-mass-damper system experiencing base excitation. (This method is similar to one suggested by Yung[27]). A schematic of the experimental model is shown in Figure A1. The displacements of the accelerometer transducer and the center of gravity of the body are denoted as X_1 and X_2 respectively. The transducer acceleration, $\ddot{X}_1$ was measured while the base acceleration, $\ddot{X}_2$, was the desired output. Since the accelerometer package accounted for less than 6% of the total system mass, the motion of the center of gravity of the sphere was assumed to be independent of the package motion. The linear equation of motion for the accelerometer package is then

$$m\ddot{X}_1=k(X_2-X_1)+c(\dot{X}_2-\dot{X}_1) \tag{A1}$$

or separating the response, X_1, from the excitation, X_2,

$$m\ddot{X}_1+c\dot{X}_1+kX_1=c\dot{X}_2+kX_2 \tag{A2}$$

where the mass of the accelerometer package is m. Define now

$$\omega_n^2=k/m \qquad c/m=2\zeta\omega_n$$

Then Eq. (A2) becomes

$$\ddot{X}_1+2\zeta\omega_n\dot{X}_1+\omega_n^2X_1=2\zeta\omega_n\dot{X}_2+\omega_n^2X_2 \tag{A3}$$

Following linear system analysis, the excitation, X_2, and the response, X_1, are related by the frequency system response function $H(\omega)$ where

$$\text{(transducer accel.)/(base accel.)}$$
$$=(-\omega^2X_1)/(-\omega^2X_2)=X_1/X_2=H(\omega) \tag{A4}$$

and, from the solution for Eq. (A3)

$$H(\omega)=\frac{i\omega 2\zeta\omega_n+\omega_n^2}{-\omega^2+i\omega 2\zeta\omega_n+\omega_n^2} \tag{A5}$$

The impulse response function, $h(t)$, is given as the Inverse Fourier Transform of $H(\omega)$. (See Kaplan (1962) or any other book on the calculus of linear systems.) It can be easily shown that the Inverse Fourier Transform of Eq. (A5) is

$$h(t)=e^{-\zeta\omega_n t}\left[2\zeta\omega_n\cos\omega_d t+\frac{\omega_n^2-2(\zeta\omega_n)^2}{\omega_d}\sin\omega_d t\right] \tag{A6}$$

where $\omega_d=\omega_n\sqrt{1-\zeta^2}$ is the damped natural frequency. The damping factor, ζ, and the damped natural frequency, ω_d, were calculated from the experimental time history.

For the linear system shown in Figure A1, the transducer acceleration, $\ddot{X}_1(t)$, is related to the base acceleration, $\ddot{X}_2(t)$, by the convolution integral

$$\ddot{X}_1(t)=\int_0^t d\tau\ h(t-\tau)\ddot{X}_2(\tau). \tag{A7}$$

In the application discussed in this paper, $\ddot{X}_1(t)$ was the measured quantity while $\ddot{X}_2(t)$, the acceleration of the body center of gravity, was the unknown. Through discretization, the following approximation for Eq. (A7) may be written:

$$\ddot{X}_1(t_k)=\sum_{j=1}^{k}\ddot{X}_2(t_j)\int_{t_{j-1}}^{t_j} d\tau h(t_k-\tau) \tag{A8}$$

The integral term in the above equation has a closed form expression. Eq. (A8) may then be inverted to yield the body acceleration $\ddot{X}_2$ at time step t_j.

One example of the data reduction technique is shown in Figure A2. There the measured impact acceleration time history is plotted with the results of Eq.(A8). The experimental accelerometer response is plotted as the solid line while the simulated base acceleration is plotted as the dashed line. The reliability of the data was established in two ways. First, the tests at the various drop heights were repeated two or three times. When superimposed upon each other, the resulting time histories showed a high degree of repeatability. Next, the results for the different drop heights, when normalized by the velocity squared, showed approximately the same maximum accelerations. See, for example, Figure 7.